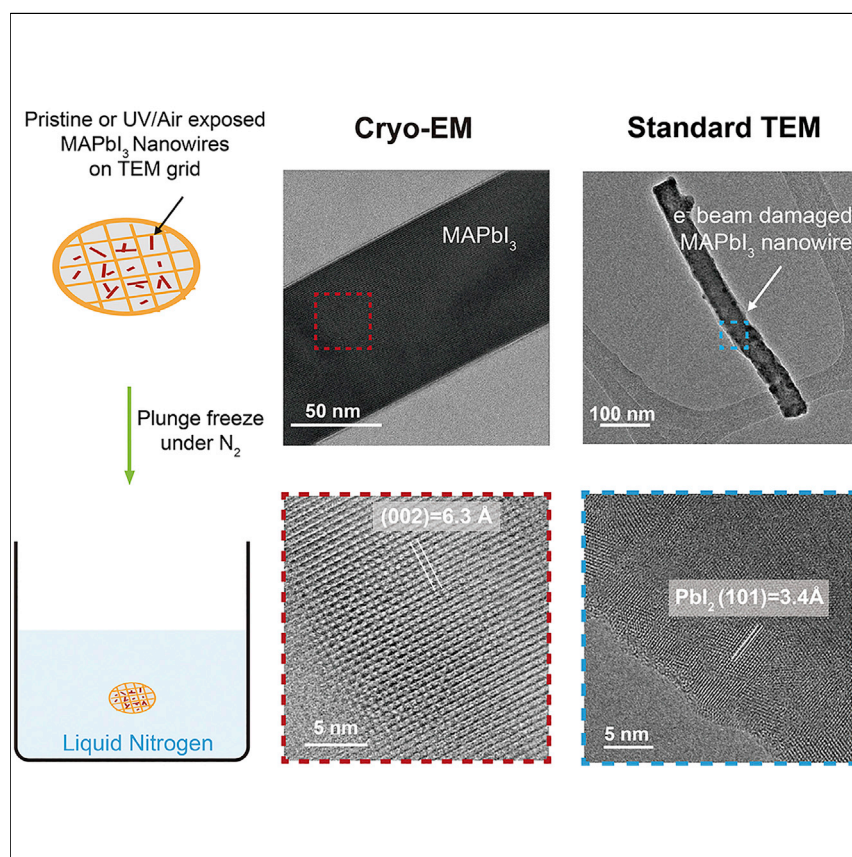


## Article

# Unravelling Degradation Mechanisms and Atomic Structure of Organic-Inorganic Halide Perovskites by Cryo-EM



As a promising candidate for efficient, scalable, and inexpensive solar cells, hybrid organic-inorganic halide perovskites have attracted tremendous research attention. However, their structural degradation during environmental exposure (e.g., UV light, moisture), which limits the commercialization of hybrid perovskites, is poorly understood. Using cryoelectron microscopy, we stabilize these electron beam-sensitive materials for atomic-scale observation and reveal the nanoscale morphology and structure by freezing these materials during the degradation (e.g., UV illumination, moisture exposure) process.

Yanbin Li, Weijiang Zhou,  
Yuzhang Li, ..., Rafael Vila, Wah  
Chiu, Yi Cui

wahc@stanford.edu (W.C.)  
yicui@stanford.edu (Y.C.)

## HIGHLIGHTS

Cryo-EM preserves and stabilizes hybrid perovskite for atomic-scale imaging

Established the definition of critical electron dose for hybrid perovskite TEM imaging

Captured the nanoscale structure changes of hybrid perovskite under degradation

Article

# Unravelling Degradation Mechanisms and Atomic Structure of Organic-Inorganic Halide Perovskites by Cryo-EM

Yanbin Li,<sup>1,7</sup> Weijiang Zhou,<sup>2,7</sup> Yuzhang Li,<sup>1,7</sup> Wenxiao Huang,<sup>1</sup> Zewen Zhang,<sup>1</sup> Guangxu Chen,<sup>1</sup> Hansen Wang,<sup>1</sup> Gong-Her Wu,<sup>3</sup> Nicholas Rolston,<sup>4</sup> Rafael Vila,<sup>1</sup> Wah Chiu,<sup>2,3,5,\*</sup> and Yi Cui<sup>1,6,8,\*</sup>

## SUMMARY

Despite rapid progress of hybrid organic-inorganic halide perovskite solar cells, using transmission electron microscopy to study their atomic structures has not been possible because of their extreme sensitivity to electron beam irradiation and environmental exposure. Here, we develop cryoelectron microscopy (cryo-EM) protocols to preserve an extremely sensitive perovskite, methylammonium lead iodide (MAPbI<sub>3</sub>) under various operating conditions for atomic-resolution imaging. We discover the precipitation of lead iodide nanoparticles on MAPbI<sub>3</sub> nanowire's surface after short UV illumination and surface roughening after only 10 s exposure to air, while these effects remain undetected in conventional X-ray diffraction. We establish a definition for critical electron dose and find this value for MAPbI<sub>3</sub> at cryogenic condition to be 12 e<sup>-</sup>/Å<sup>2</sup> at 1.49 Å spatial resolution. Our results highlight the importance of cryo-EM since traditional techniques cannot capture important nanoscale changes in morphology and structure that have important implications for perovskite solar cell stability and performance.

## INTRODUCTION

Hybrid organic-inorganic halide perovskite solar cells (PSCs) have attracted tremendous research attention and quickly dominated photovoltaic (PV) research for a number of reasons. As a solution-processable material, hybrid perovskite (CH<sub>3</sub>NH<sub>3</sub>PbI<sub>3</sub>, MAPbI<sub>3</sub>) has the potential to deliver efficient, scalable, and inexpensive solar energy.<sup>1–4</sup> The first solar cell employing hybrid perovskite was reported in 2009 with a power conversion efficiency (PCE) of 3.81%.<sup>5</sup> In just one decade, PSCs have now reached a PCE > 24%, which is comparable to that of silicon-based solar cells that have enjoyed many decades of development.<sup>2–4</sup> Despite the rapid growth in performance efficiency, the commercial deployment of PSCs is hindered by their poor stability under practical operating conditions.<sup>3,6–8</sup>

As illustrated in Figure 1A, PSCs have been reported to decompose into precursor materials upon exposure to common environmental conditions such as moisture,<sup>6</sup> local heating,<sup>9</sup> and ultraviolet (UV) illumination.<sup>10–12</sup> Other phenomena such as oxygen interpenetration and illumination-induced ion migration<sup>13,14</sup> not only diminish material stability by structural deformation but also lead to anomalous hysteresis in current-voltage curves that are not yet fully understood. Despite significant research activity directed toward the application of PSCs, the atomic- and nanoscale understanding of how degradation conditions change the crystal structure, morphology, and physical properties of hybrid perovskite remains

## Context & Scale

As the hybrid perovskite-based solar cell and light emitting diode (LED) efficiencies rapidly increase, elucidating nanoscale degradation mechanisms of hybrid perovskite becomes very important for the development of strategies towards highly efficient and stable perovskite-based optoelectronic devices. Previous attempts using transmission electron microscopy have not been possible because of their extreme sensitivity to electron beam irradiation and environmental exposure. Here, we develop cryoelectron microscopy (cryo-EM) protocols to preserve an extremely sensitive perovskite, methylammonium lead iodide, under various operating conditions for atomic-resolution imaging. Meanwhile, we establish a definition for critical electron dose to avoid electron-beam-induced damage during the imaging process. The cryo-EM protocols established in this work will enable a broad area of investigation into the atomic-scale operating and failure modes in perovskite solar cell and LED research.

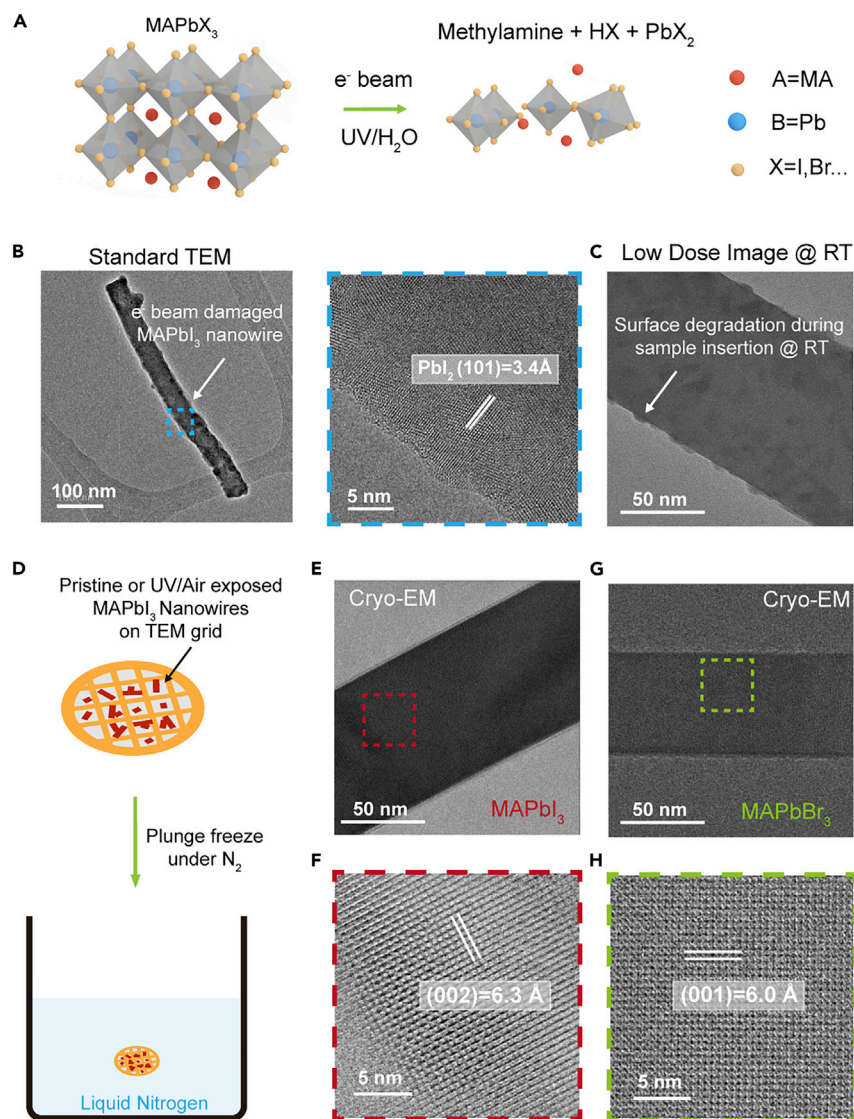


**Figure 1. Preserving and Stabilizing Hybrid Perovskite Using Cryo-EM**

(A) Upon exposure to e-beam, UV, or moisture, hybrid perovskites decompose into the precursor materials.

(B) Standard TEM image of MAPbI<sub>3</sub> NWs. After exposure to electron dose  $\sim 500 \text{ e}^-/\text{\AA}^2$ , MAPbI<sub>3</sub> decomposes into PbI<sub>2</sub>.

(C) Low-dose image of MAPbI<sub>3</sub> NW inserted into TEM by standard TEM sample loading procedure at room temperature. NW surface roughening confirms the degradation during room temperature sample insertion.

(D) Pristine or UV/moisture exposed perovskite NWs were dropcast onto a quantifoil TEM grid in nitrogen glovebox. Then, the sample was plunge-frozen into liquid nitrogen inside glovebox.

(E and G) TEM images of MAPbI<sub>3</sub> (E) and MAPbBr<sub>3</sub> (G) show smooth surface on NWs.

(F and H) Atomic-resolution TEM images resolving [PbI<sub>6</sub>]<sup>4-</sup> octahedral and MA<sup>+</sup> molecule of MAPbI<sub>3</sub> (F) and MAPbBr<sub>3</sub> (H).

Electron dose is  $\sim 12 \text{ e}^-/\text{\AA}^2$  in (C) and (F) and  $\sim 46 \text{ e}^-/\text{\AA}^2$  in (H).

elusive. Therefore, it is critical to develop methods for revealing the atomic structure of PSCs at various operating conditions to provide insight into addressing important issues with stability and pave the way for commercialization of perovskite optoelectronic devices.

<sup>1</sup>Department of Materials Science and Engineering, Stanford University, Stanford, CA 94305, USA

<sup>2</sup>Biophysics Program, School of Medicine, Stanford University, Stanford, CA 94305, USA

<sup>3</sup>Department of Bioengineering, Stanford University, Stanford, CA 94305, USA

<sup>4</sup>Department of Applied Physics, Stanford University, Stanford, CA 94305, USA

<sup>5</sup>Division of CryoEM and Bioimaging, SSRL, SLAC National Accelerator Laboratory, Menlo Park, CA 94025, USA

<sup>6</sup>Stanford Institute for Materials and Energy Sciences, SLAC National Accelerator Laboratory, 2575 Sand Hill Road, Menlo Park, CA 94025, USA

<sup>7</sup>These authors contributed equally

<sup>8</sup>Lead Contact

\*Correspondence: [wahc@stanford.edu](mailto:wahc@stanford.edu) (W.C.), [yicui@stanford.edu](mailto:yicui@stanford.edu) (Y.C.)

<https://doi.org/10.1016/j.joule.2019.08.016>

Unfortunately, current understanding of degradation mechanisms is largely limited to ensemble studies using X-ray/neutron diffraction,<sup>15–17</sup> selected area electron diffraction (SAED),<sup>18,19</sup> and surface-sensitive techniques.<sup>10</sup> Although transmission electron microscopy (TEM) has been used to study the macroscopic morphology of PSCs, atomic-resolution imaging remains challenging due to its extreme sensitivity to electron beam damage.<sup>9</sup> By imaging at ultralow electron dose ( $11 \text{ e}^-/\text{\AA}^2$ ), Han et al. successfully acquired a high-resolution TEM (HRTEM) image of a bromide-based perovskite ( $\text{MAPbBr}_3$ ) at room temperature.<sup>20</sup> However,  $\text{MAPbBr}_3$  remains an inefficient perovskite solar cell material with limited application due to its large band gap. In contrast, the iodide-based perovskite ( $\text{MAPbI}_3$ ) is much more efficient yet cannot be imaged as readily with atomic resolution since it is much more sensitive than  $\text{MAPbBr}_3$ , creating an extreme challenge for TEM imaging.

Recently, cryoelectron microscopy (cryo-EM) was shown to be a powerful tool beyond structural biology. In particular, reactive and electron beam-sensitive lithium battery materials have been successfully stabilized for TEM sample loading, imaging, and spectroscopy.<sup>21–26</sup> We hypothesize that such a cryogenic condition may also reduce electron beam damage to hybrid perovskites such as  $\text{MAPbI}_3$ . Here, we establish a cryo-EM protocol to successfully reveal the atomic structure of  $\text{MAPbI}_3$  and quantify its cryogenic critical dose to be  $12 \text{ e}^-/\text{\AA}^2$  at  $1.49 \text{ \AA}$  spatial resolution. We also measured the critical dose of  $\text{MAPbBr}_3$  to be  $46 \text{ e}^-/\text{\AA}^2$ , which is improved by 4 times compared to room temperature condition (only  $11 \text{ e}^-/\text{\AA}^2$ ) in a previous study.<sup>20</sup> We measured that the electron dose tolerance of  $\text{MAPbI}_3$  is much lower than  $\text{MAPbBr}_3$  at the cryogenic condition. Furthermore, cryogenic conditions enable preservation of the pristine or degraded  $\text{MAPbI}_3$  structure during various durations of UV light or moisture exposure. Therefore, the cryo-EM methodology developed in this study enables our investigation into the nanoscopic decomposition pathways of  $\text{MAPbI}_3$  and enables correlating nanostructure with macroscopic device performance.

## RESULTS AND DISCUSSION

### Cryo-EM Imaging for Hybrid Perovskite

Hybrid perovskites possess an  $\text{ABX}_3$  structure, where A usually contains an organic cation ( $\text{MA}^+$  = methylammonium), B is a divalent metal cation ( $\text{Pb}^{2+}$ ), and X is a halide anion ( $\text{I}^-$ ,  $\text{Br}^-$ , or  $\text{Cl}^-$ ) (Figure 1A). The vast majority of PSCs comprise a thin film geometry, where a polycrystalline thin film (>300 nm) is formed with a wide range of processing methods, microstructures, and precursors. However, there is still a lack of mechanistic understanding on the control of film crystallinity and morphology. Additionally, optoelectronic properties have been shown to depend on perovskite composition<sup>27</sup> and grain boundaries.<sup>28</sup> Single crystals of pure  $\text{MAPbX}_3$  have not only been shown to exhibit among the lowest defect densities and highest charge carrier diffusion lengths,<sup>29</sup> but they also involve the simplest perovskite structure that is most commonly used in literature for high-efficiency solar cells.<sup>30</sup> Due to the existence of heavy Pb atoms, a suitable perovskite TEM sample should not be thicker than 100 nm. In addition, a previous study has successfully demonstrated the fabrication of effective solar cells based on perovskite nanowires (NWs).<sup>31</sup> As a result, single-crystal  $\text{MAPbI}_3$  NWs were chosen as a convenient model system to study the nanoscale degradation mechanisms of the solar cell material.

To exclude the effect from surface ligand,<sup>8</sup> in this study,  $\text{MAPbI}_3$  nanowires were synthesized on glass substrates using a previously reported ligand-free method<sup>32</sup> inside a nitrogen glovebox. The split of the (220) and (004) peaks in powder X-ray

diffraction (XRD) (Figure S1) pattern indicates a pure tetragonal MAPbI<sub>3</sub> crystal structure (space group *I4/mcm*,  $a = 8.896 \text{ \AA}$ ,  $c = 12.707 \text{ \AA}$ ), rather than the high-temperature cubic phase.<sup>33</sup> No residue PbI<sub>2</sub> precursor is observed. MAPbBr<sub>3</sub> NWs were synthesized by replacing MAI precursor with MABr. The XRD patterns show that the as-grown NWs are cubic-phase MAPbBr<sub>3</sub> (space group *Pm3m*) without impurities (Figure S2). However, as shown in Figure 1B, MAPbI<sub>3</sub> NWs quickly decompose into PbI<sub>2</sub> upon exposure to high electron dose ( $500 \text{ e}^-/\text{\AA}^2$ ) during TEM imaging at room temperature due to extreme electron beam sensitivity of the organic MA<sup>+</sup> cation. Previous TEM studies on MAPbI<sub>3</sub> were usually conducted under low magnification using SAED with a carefully tuned low electron dose rate of only  $1 \text{ e}^-/\text{\AA}^2\text{s}^{-1}$  to avoid potential beam damage at room temperature.<sup>18,19</sup> In addition, the short (<5 s) air exposure during standard TEM sample insertion will expose MAPbI<sub>3</sub> NWs to moisture. As shown in Figure 1C, after standard TEM sample insertion procedure, the MAPbI<sub>3</sub> NW was imaged with an electron dose of  $\sim 12 \text{ e}^-/\text{\AA}^2$  to avoid beam damage. A clear surface roughening is observed, which demonstrates the surface degradation during sample insertion.

To overcome the particular electron beam and moisture sensitivity of perovskite solar cell materials, we engineered a plunge-freezing procedure modified from cryo-EM methodologies used in structural biology<sup>34</sup> to preserve the hybrid perovskites in their pristine or operating state for high-resolution imaging (Figure 1D). First, the as-grown perovskite NWs were dropcast onto a Quantifoil TEM grid in an inert environment. Then, the sample was plunge-frozen into liquid nitrogen in the glovebox. Side reactions between hybrid perovskites and nitrogen or moisture is kinetically inhibited at cryogenic temperatures, which allows the plunge-freezing process to retain the original state of the hybrid perovskite NWs with the relevant structural information successfully preserved. To study the nanoscale degradation mechanism under independent UV light radiation or moisture exposure, we subjected samples to UV illumination (Figure S3) inside an Ar-filled glovebox or in ambient air (relative humidity  $\sim 40\%$ ) before plunge-freezing. The sample was then transferred into the TEM column (operating at 200 kV) without any air exposure and kept at  $-175^\circ\text{C}$  for TEM imaging using a direct-detection electron-counting camera (DDEC).<sup>35</sup> With the high quantum detective efficiency in the counting mode of DDEC, images can be acquired under extremely low dose. In addition to electron beam damage, HRTEM of beam-sensitive materials often suffers from beam-induced sample motion, which blurs the image.<sup>36</sup> With the high detective quantum efficiency of DDEC, we were able to acquire images by breaking down the total dose into a successive series of low-dose frames followed by subsequent frame alignment to minimize this motion<sup>36</sup> (see Experimental Procedures).

Figure 1E is a typical cryo-HRTEM image of MAPbI<sub>3</sub> NW taken at the magnification of 80,000 corresponding to a pixel size of  $0.46 \text{ \AA}$  by  $0.46 \text{ \AA}$ . In general, sample regions were exposed to an electron dose of  $\sim 12 \text{ e}^-/\text{\AA}^2$  to avoid beam damage. We noticed that higher electron dose may induce sample damage through the formation of methylamine or halogen bubbles<sup>37</sup> (Figure S4), which is not observed at room temperature. In contrast to beam-damaged MAPbI<sub>3</sub> NWs under standard room temperature TEM conditions, NWs imaged at cryogenic conditions have a much smoother surface. High-resolution images of MAPbI<sub>3</sub> NWs (Figure 1F) resolve individual [PbI<sub>6</sub>]<sup>4-</sup> octahedral and MA<sup>+</sup> molecule column, showing that perovskite NWs are single crystalline. Image simulation confirms that the areas of bright contrast correspond to MA molecule columns (Figures S5 and S6). A series of fast Fourier transform (FFT) of the MAPbI<sub>3</sub> image (Figure 2A) shows structural information down to  $1.49 \text{ \AA}$ . It has been reported that MAPbI<sub>3</sub> undergoes an equilibrium phase transition from

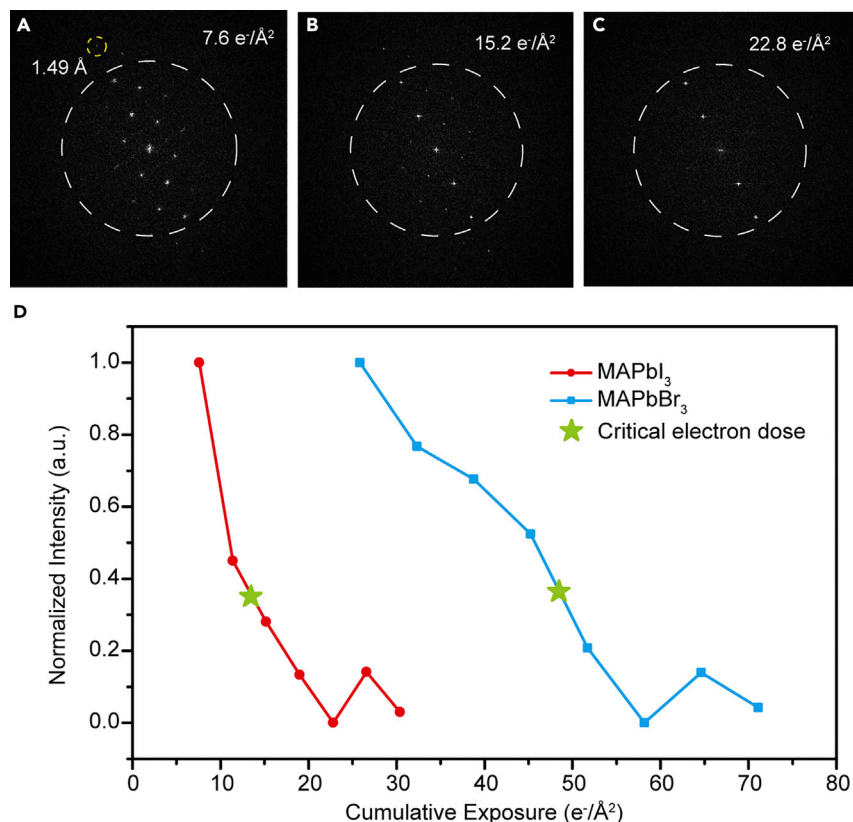


### Figure 2. Radiation Damage Measurement and Quantification

(A–C) Fast Fourier transform of MAPbI<sub>3</sub> HRTEM images with cumulative electron exposure 7.6 e<sup>-</sup>/Å<sup>2</sup> (A), 15.2 e<sup>-</sup>/Å<sup>2</sup> (B), and 22.8 e<sup>-</sup>/Å<sup>2</sup> (C). Yellow circle in (A) shows that information as low as 1.49 Å is preserved. White dashed circle represents a resolution and information transfer of 2 Å.

(D) Normalized intensity of diffraction spots with lattice spacing less than 2 Å versus cumulative electron exposure for MAPbI<sub>3</sub> (red) and MAPbBr<sub>3</sub> (blue). Electron dose that decreased normalized intensity to 30% from its maximum is marked with a star as critical electron dose for HRTEM imaging. Dose rate of 3.8 e<sup>-</sup> Å<sup>-2</sup> s<sup>-1</sup> is used for MAPbI<sub>3</sub>, and 25.6 e<sup>-</sup> Å<sup>-2</sup> s<sup>-1</sup> is used for MAPbBr<sub>3</sub>.

tetragonal to orthorhombic at ~165 K.<sup>17,38</sup> However, based on HRTEM images and the FFT (Figures 1F and 2A), this structural change is not observed likely due to the fast cooling of our plunge-freezing procedure, further demonstrating that the native state of our material (tetragonal phase) can be successfully preserved. In addition, HRTEM images of MAPbBr<sub>3</sub> and mixed halide MAPb(Br<sub>0.5</sub>I<sub>0.5</sub>)<sub>3</sub> NWs were taken at the same magnification (Figures 1G and S7). We found that typically MAPbBr<sub>3</sub> and MAPb(Br<sub>0.5</sub>I<sub>0.5</sub>)<sub>3</sub> NWs are over 4 times more tolerant to electron beam exposure than MAPbI<sub>3</sub>. Thus, to minimize the dose rate for different perovskites and establish a standard for electron dose accumulation, we performed an electron dose tolerance test that dictates the ideal electron dose exposure for each material in our study.

### Radiation Damage Measurement and Quantification

Electron beam damage has been investigated rigorously in biological cryo-EM as it is the fundamental factor that limits the resolution of frozen-hydrated specimens.<sup>39</sup> Here, we extend the electron radiation damage evaluation methodology from biological cryo-EM to the beam-sensitive hybrid perovskite. With the aid of the electron counting mode of DDEC, the electron dose rate (e<sup>-</sup> Å<sup>-2</sup> s<sup>-1</sup>) of certain illumination

conditions can be characterized. A slightly longer exposure time, typically 3–4 s, was chosen to record a multiple-frame image stack. Figures 2A–2C are a stack of successive FFT of MAPbI<sub>3</sub> NWs HRTEM images during a dose tolerance test (7.6, 15.2, and 22.8 e<sup>-</sup>/Å<sup>2</sup>). The white dashed circle represents an information transfer of 2 Å. When the number of frames taken and the cumulative electron exposure is increased, MAPbI<sub>3</sub> shows a partial loss of crystallinity (15.2 and 22.8 e<sup>-</sup>/Å<sup>2</sup> in Figures 2B and 2C, respectively).

Furthermore, the intensity of diffraction spots in FFT with lattice spacing less than 2 Å was extracted and normalized for quantitative analysis. Figure 2D shows the plot of normalized intensity as a function of cumulative electron exposure. The fluctuation of normalized intensity after long-term electron beam exposure is attributed to background noise. Based on this plot, we define the electron dose that decreased normalized intensity to 1/e from its maximum as the critical HRTEM imaging dose for perovskite, which is ~12 e<sup>-</sup>Å<sup>-2</sup> in the case of MAPbI<sub>3</sub> (marked by a star in Figure 2D). It is worth mentioning that under this definition, the information higher than 2 Å is still preserved as shown in Figure 2B, corresponding to 15.2 e<sup>-</sup>Å<sup>-2</sup> cumulative electron exposure. Similarly, a dose tolerance test was performed on MAPbBr<sub>3</sub> NWs (Figure S8). Indeed, as shown in Figure 2D, MAPbBr<sub>3</sub> has a higher electron beam tolerance compared to MAPbI<sub>3</sub>. Following the same definition, we identify 46 e<sup>-</sup>Å<sup>-2</sup> as the critical dose for MAPbBr<sub>3</sub>, which is 4 times higher than the electron dose reported previously.<sup>20</sup>

### Exposure to UV Irradiation

Prolonged exposure of MAPbI<sub>3</sub> to UV light irradiation has been previously shown to decompose the material into PbI<sub>2</sub> via a free electron mechanism involving the TiO<sub>2</sub> conduction layer.<sup>11</sup> The stability of MAPbI<sub>3</sub> on nonconductive substrates like Al<sub>2</sub>O<sub>3</sub> is believed to be much improved based on XRD characterization.<sup>12</sup> However, the nanoscale degradation mechanism of MAPbI<sub>3</sub> remains elusive. Unfortunately, probing the nanoscale structure involved in this degradation process requires high spatial resolution techniques using electron microscopy. Previous studies have been inconclusive because it has not been possible to deconvolute the effect of the electron beam from the UV light degradation, both of which decompose the MAPbI<sub>3</sub> to PbI<sub>2</sub>.

Using our cryo-EM methodology, we tested the intrinsic UV light stability of MAPbI<sub>3</sub> NWs without the addition of any charge transport layers (e.g., TiO<sub>2</sub>). XRD spectra of MAPbI<sub>3</sub> NWs after broadband UVA light exposure in an argon environment for 0 min (pristine), 15 min, 30 min, and 60 min were collected (Figure 3A). These short exposure times did not form any detectable PbI<sub>2</sub> peaks (black PbI<sub>2</sub> reference curve in Figure 3A) in the XRD dataset. Furthermore, 60 min UV illuminated MAPbI<sub>3</sub> NWs were loaded on silicon (100) substrate for XRD fine scanning around PbI<sub>2</sub> peak positions. As shown in Figure S9, no PbI<sub>2</sub> peak was detected. Therefore, these data show that the MAPbI<sub>3</sub> NWs are stable after the short UV light illumination, especially because there is no TiO<sub>2</sub> layer. However, when the above UV-exposed MAPbI<sub>3</sub> NWs are investigated using the established cryo-EM methodologies and protocols described above, we discover an obvious change in nanowire surface morphology visible as dark contrast region (~5 nm) in the nanowire image that was not observed using conventional characterization methods (Figure 3B).

This morphology is markedly different from the pristine case when not exposed to UV light (Figure 1D). These dark contrast features continue to grow larger with increasing UV exposure (Figures 3C and 3D) within the time of our investigations. When examining the regions of dark contrast at a higher magnification, we can

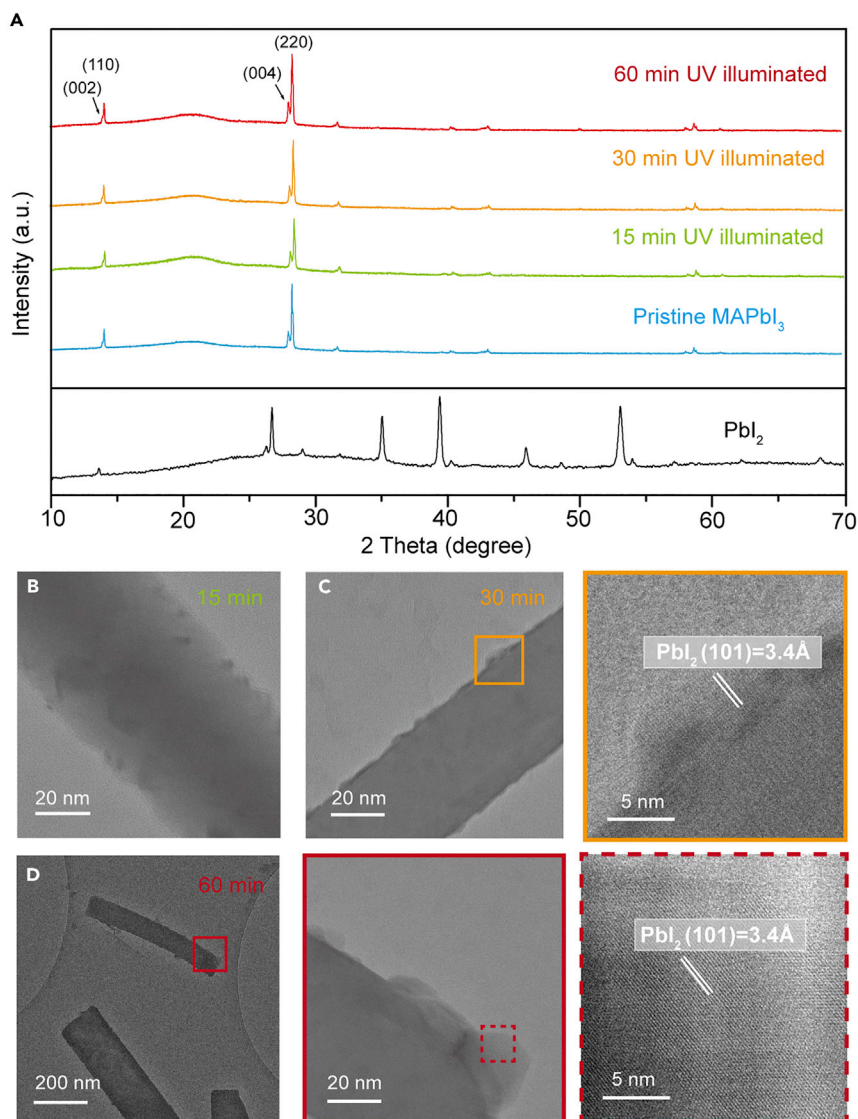


**Figure 3. MAPbI<sub>3</sub> Degradation under UV Light Radiation**

(A) XRD spectra of MAPbI<sub>3</sub> after 0 min (pristine), 15 min, 30 min, and 60 min of UV illumination. No PbI<sub>2</sub> peaks (curve in black) are detected within an hour of UV illumination.

(B–D) Cryo-EM images of MAPbI<sub>3</sub> NW after 15 min (B), 30 min (C), and 60 min (D) of UV illumination. Nanograins of crystalline PbI<sub>2</sub> are clearly resolved on the surface of the MAPbI<sub>3</sub> NW.

resolve atomic crystalline structures that correspond to the (110) lattice spacing of PbI<sub>2</sub> (PDF No. 07-0235). Our observation provides new insight to previous XRD studies that suggest PbI<sub>2</sub> would not be formed at short exposure times. In previous room temperature TEM experiments, this observation would be attributed to artifacts generated by the electron-beam-induced degradation of the MAPbI<sub>3</sub> material. However, the cryo-EM methodology used in this study with a critical dose limited to 12 e<sup>-</sup>Å<sup>-2</sup> ensures that our observation remains an accurate reflection of the NWs' states preserved during cryogenic freezing without the concern of artifacts generated by the imaging technique.

There are several important implications of this new discovery. First, this degradation under short UV light exposure is unexpected and surprising because it could

not be detected using previous techniques like XRD or UV-vis spectroscopy. This may be because the nanograins of  $\text{PbI}_2$  are too small (5 nm) and the number density is too low for XRD to detect. Thus, the apparent formation of  $\text{PbI}_2$  could also influence the opto-electronic properties of the  $\text{MAPbI}_3$ , which was previously thought to be pristine. Second, the fact that this degradation occurs without the presence of  $\text{TiO}_2$  suggests an entirely different degradation mechanism is at play when UV light is illuminated onto  $\text{MAPbI}_3$  and implies that the material is intrinsically unstable. One initial hypothesis is that the UV light triggers a structural degradation in the sensitive organic-inorganic bonds, collapsing the framework structure and accelerating the decomposition back into the  $\text{PbI}_2$  starting material. Finally, the apparent presence of  $\text{PbI}_2$  decomposition product under such short UV exposure times could have an impact on the performance of individual devices and could potentially explain the broad range of device efficiencies within even the same batch. Additionally, there is a commonly reported effect of early-time light-induced degradation or “burn-in” reported during initial solar cell operation<sup>40</sup>—the mechanism for which remains unknown—which may be related to the morphological changes observed by cryo-EM. This new finding has important implications for the performance of this important solar cell material and highlights the potential impact of new discoveries using nanoscale studies on degradation mechanisms enabled by our cryo-EM protocol.

### Exposure to Moisture Environment

Moisture sensitivity of  $\text{MAPbI}_3$  also limits its long-term stability and has been shown to greatly degrade device performance.<sup>7</sup> Many theories on the degradation mechanism have been proposed based on the chemical reactions with water and oxygen but are largely limited by the lack of nanoscale information. Conventional techniques like XRD that measure the average ensemble structure may not detect important nanoscale changes, as shown above for UV irradiation. Previous studies have shown that the  $\text{MAPbI}_3$  XRD peak disappears after exposure to moisture on the time-scale of days ( $\sim 24$  h).<sup>8</sup> However, an atomic level picture of the initial degradation process is lacking.

To reveal the nanoscale degradation process of  $\text{MAPbI}_3$  NWs, we exposed  $\text{MAPbI}_3$  NWs to air with 40% relative humidity at room temperature for short durations before plunge-freezing into liquid nitrogen to preserve its degraded state. Optically, the color change from dark brown to yellow indicates full decomposition of the  $\text{MAPbI}_3$  after 2 days of moisture exposure (Figure 4A). At shorter exposure times of 10 s, 45 min, and 2 h, no change can be detected optically and  $\text{PbI}_2$  peaks indicative of degradation remain absent in XRD spectra (Figure S10), which would suggest the  $\text{MAPbI}_3$  NWs remain stable. In contrast, high-resolution cryo-EM images uncover the initial nanoscale degradation process that cannot be detected using conventional techniques. Surprisingly, even with only 10 s of moisture exposure, a clear roughening of the surface is observed (Figures 4B and 4C). This extreme sensitivity in air is likely due to the lack of surface-protecting ligands during the synthesis of these perovskite NWs, which means that a standard TEM procedure could cause artifacts during perovskite sample loading.

After 45 min of moisture exposure, a thin amorphous layer ( $\sim 5$  nm) appears on the surface of the  $\text{MAPbI}_3$  nanowire (Figures 4D and 4E). The amorphous material could be a hydrated compound that forms when exposed to water vapor.<sup>7</sup> The FFT of the  $\text{MAPbI}_3$  (Figure 4D, inset) indicates that the crystallinity of the nanowire as a whole has not been damaged, yet the surface is clearly degraded. This could have important implications on the charge-transport phenomenon at the surface of  $\text{MAPbI}_3$  and

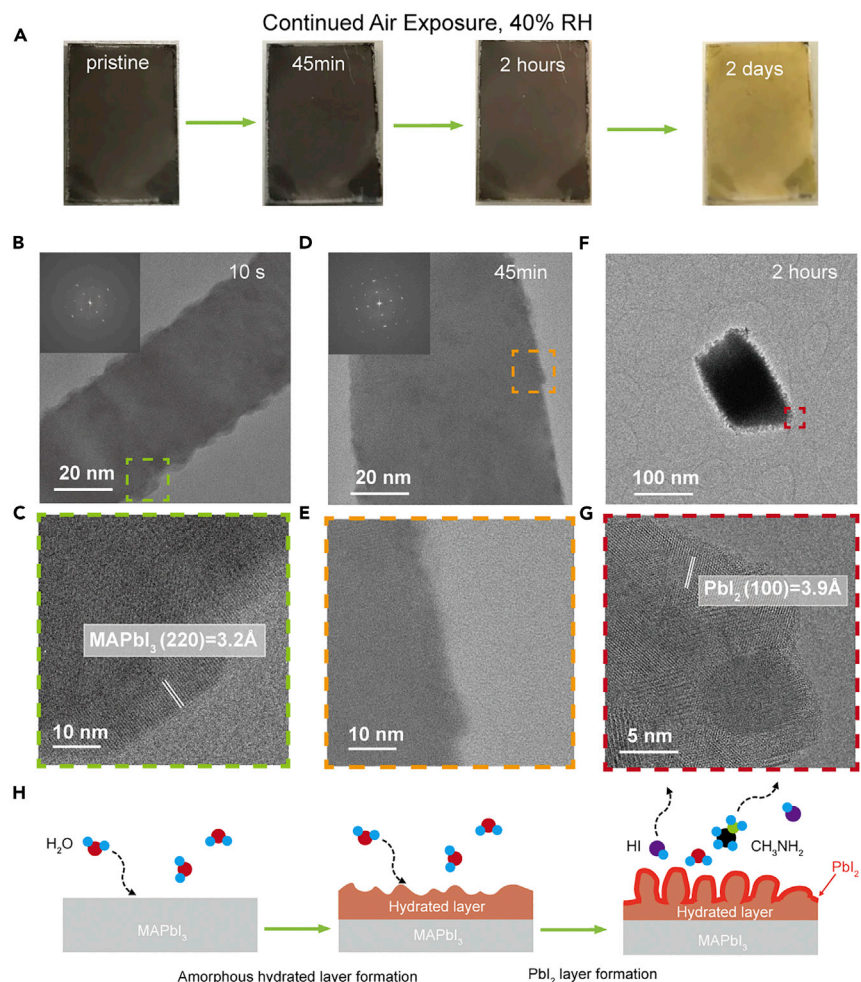


#### Figure 4. MAPbI<sub>3</sub> Degradation under Moisture Exposure

(A) Optical images of MAPbI<sub>3</sub> NW films taken at various exposure durations in air with 40% relative humidity at room temperature. Color change is visible after 2 days.

(B–G) Cryo-EM images of MAPbI<sub>3</sub> NWs after 10 s (B and C), 45 min (D and E), and 2 h (F and G) of moisture exposure. (B) Cryo-EM image of MAPbI<sub>3</sub> NWs after 10 s. (C) Zoomed-in region of (B). (D) Cryo-EM image of MAPbI<sub>3</sub> NWs after 45 min. (E) Zoomed-in region of (D). (F) Cryo-EM image of MAPbI<sub>3</sub> NWs after 2 h. (G) Zoomed-in region of (F).

(H) Schematic of proposed nanoscale degradation mechanism of MAPbI<sub>3</sub> in moisture environment: a thin amorphous film (~5 nm) initially forms on the surface of the MAPbI<sub>3</sub> that facilitates further decomposition into PbI<sub>2</sub> and other components (e.g., HI and CH<sub>3</sub>NH<sub>2</sub>).

its interface with charge carrier conduction layers. Light harvesting would also change with the growth of this amorphous film upon exposure to moisture. After 2 h of moisture exposure, cryo-EM images show that the MAPbI<sub>3</sub> NW surface has noticeably become rougher with the presence of whisker-like structures sticking out (~30 nm) (Figures 4F and 4G). High-resolution images reveal that these nanoscale whiskers contain nanograins of PbI<sub>2</sub> (~5 nm) dispersed in the amorphous layer observed as in Figure 4D, indicating that the degradation process has progressed after only 2 h of moisture exposure.

The high-resolution studies of moisture-induced MAPbI<sub>3</sub> degradation enabled by cryo-EM suggest a nanoscale degradation pathway (Figure 4H). Initially, an amorphous layer likely consisting of a hydrated compound coats the MAPbI<sub>3</sub> surface. This thin layer

then facilitates decomposition of the  $\text{MAPbI}_3$  into gaseous components (e.g., HI and  $\text{CH}_3\text{NH}_2$ ) and nanograins of  $\text{PbI}_2$ , further roughening the surface of the remaining  $\text{MAPbI}_3$  material. Interestingly, this degradation proceeds under much milder conditions (no UV irradiation, room temperature) than previous studies, which could have important implications on materials processing protocols and requirements for device sealing to minimize exposure to moisture. This result could explain why some of the most stable reported solar cells use procedures that eliminate moisture exposure by depositing *in situ* barrier layers<sup>41</sup> or encapsulating in inert environments.<sup>42</sup>

### Outlook and Conclusion

The protocols established in this study introduce a specimen preparative method for sensitive materials systems like hybrid PSCs under experimentally defined environmental conditions including UV illumination and moisture exposure. By engineering the freezing process to preserve the authentic nanostructures at nanoscale and closely monitoring the cumulative electron exposure to minimize its radiation damage effects, we successfully retrieve the structure signatures of  $\text{MAPbI}_3$  solar cell materials at atomic-resolution level. Single crystal  $\text{MAPbI}_3$  NWs were used as a model system to develop a fundamental understanding of degradation without the confounding effects of grain boundaries and to maximize interface area. The next step characterizing perovskite devices with cryo-EM will leverage a process for cross-sectioning full perovskite devices using a cryo-focused-ion beam (cryo-FIB) process that has been widely applied in the biology field. This will enable the observation of device-specific degradation modes that result from operational conditions, such as interface chemistry, halide segregation in solar cells, and halide exchange in LEDs. The developed protocol will open up future studies of more complex perovskite materials (i.e., 2D Ruddlesden-Popper perovskites) for optoelectronic applications and other electron-beam-sensitive materials with unprecedented understanding of their atomic-scale structures and chemistries.

## EXPERIMENTAL PROCEDURES

### Synthesis of Hybrid Perovskite Nanostructures

First, lead iodide ( $\text{PbI}_2$ ) was spin-coated onto a glass slide (1 cm × 1.5 cm) at 3,000 rpm for 30 s from a solution of 400 mg/mL  $\text{PbI}_2$  (99.99% TCI) in dimethylformamide (DMF). Then, inside a nitrogen glovebox, the  $\text{PbI}_2$ -coated glass slide was immersed into 2 mL  $\text{CH}_3\text{NH}_3\text{I}$  (MAI),  $\text{CH}_3\text{NH}_3\text{Br}$  (MABr), or  $\text{MAI}_{0.5}\text{Br}_{0.5}$  precursor solution, with  $\text{PbI}_2$  side facing up, to synthesize  $\text{MAPbI}_3$ ,  $\text{MAPbBr}_3$ , and  $\text{MAPb}(\text{I}_{0.5}\text{Br}_{0.5})_3$  NWs, respectively. The precursor solution was prepared by dissolving MAI, MABr, or  $\text{MAI}_{0.5}\text{Br}_{0.5}$  isopropanol (IPA) with a concentration of 20 mg/mL. Before spin coating, the substrates were sequentially cleaned in ultrasonic baths of Extran 300 detergent (diluted 1:10 in deionized [DI] water), DI water, acetone, and IPA followed by 15 min of UV-ozone treatment (Jelight UVO-Cleaner Model 42).  $\text{PbI}_2$ -coated glass was heated at 100°C inside a nitrogen glovebox to remove the remnant solvent and water before being placed into the precursor solution. After 12 h, the glass substrate was removed and rinsed with 1 mL anhydrous isopropanol (Sigma-Aldrich) to remove any leftover salt on the surface, dried under a stream of nitrogen flow, and then dried on a hot plate at 100°C for another 30 s.

### X-Ray Diffraction

As-synthesized or UV-illuminated perovskite nanowires on glass were sealed with Kapton tape to avoid degradation from moisture during X-ray diffraction measurement. Then,  $\theta$ - $2\theta$  measurements were performed using a Panalytical X'Pert Pro Diffractometer (copper anode,  $K\alpha_1 = 1.54060 \text{ \AA}$ ,  $K\alpha_2 = 1.54443 \text{ \AA}$ ,  $K\alpha_2 / K\alpha_1$  ratio = 0.50).

### Electron Microscopy and Data Processing

Room temperature TEM characterizations were carried out using a FEI Titan 80-300 environmental TEM operated at 200 kV. All cryo-EM experiments were performed on a Thermo Fisher Tecnai F20 transmission electron microscope operated at 200 kV. Cryo-TEM images were acquired by a Gatan K2 direct-detection camera in the electron-counting mode with the dose fractionation function. Considering the radiation sensitivity of the material, continuous exposure to adjust defocus is impractical. Multiple short time exposure single-frame shots were taken to estimate the defocus and make it as close as possible to Scherzer defocus. Following the established data processing procedures in the latest cryo-EM makes this method more generalizable and accessible. Dose fraction frames were motion corrected by MotionCor2<sup>43</sup> to correct beam-induced movements (Figure S11). The conditions of defocus and astigmatism are determined by CTFIND4<sup>44</sup> and GCTF<sup>45</sup> followed by a manual examination. The motion-corrected images were then phase flipped by a set of MRC programs<sup>46</sup> that used to handle 2D protein crystal cryo-TEM images in traditional 2D electron crystallography. All above procedures can be done in a modern software package FOCUS<sup>47</sup> with a user-friendly GUI or separately. The amplitude correction is not included in our CTF correction to avoid artificial effects. Finally, the CTF-corrected images were denoised by a Wiener filter and an Average Background Subtraction Filter (ABSF)<sup>48</sup> that is commonly used in HRTEM to give better results. Both filters were applied to every image to avoid potential artifacts introduced by a specific filter. EMAN2<sup>49</sup> was utilized to sum up subsequent subsets of frames according to their exposure time from motion-corrected image stack, during radiation damage measurement and quantification. In our study, we summed every 5 frames per subset in the image stack. Intensity of diffraction spots in certain resolution shell in Fourier power spectrum was extracted and measured. The measured Fourier intensities were normalized by Minmax normalization. Minmax normalization is a normalization strategy that linearly transforms  $x$  to  $y = (x - \min) / (\max - \min)$ , where  $\min$  and  $\max$  are the minimum and maximum values in  $X$ , where  $X$  is the set of observed values of  $x$ .

### SUPPLEMENTAL INFORMATION

Supplemental Information can be found online at <https://doi.org/10.1016/j.joule.2019.08.016>.

### ACKNOWLEDGMENTS

The authors thank Dave Bushnell and Dong-Hua Chen for training at the Stanford-SLAC cryo-EM facilities. Yanbin Li acknowledges Robert Sinclair for helpful discussions. Yuzhang Li acknowledges the Intelligence Community Postdoctoral Research Fellowship for funding. Part of this work was performed at the Stanford Nano Shared Facilities (SNSF), supported by the National Science Foundation under award ECCS-1542152. W.C. acknowledges support by the NIH under grant nos. P41GM103832 and S10OD021600. Y.C. acknowledges support from the Assistant Secretary for Energy Efficiency and Renewable Energy, Office of Vehicle Technologies, Battery Materials Research (BMR) and Battery 500 Program of the U.S. Department of Energy.

### AUTHOR CONTRIBUTIONS

Yanbin Li, and Y.C. conceived the idea and designed the experiments. Yanbin Li and Yuzhang Li established the cryo-plunging methodologies. Yanbin Li, W.H., and G.C. synthesized the hybrid perovskite. Yanbin Li, W.Z., and G.-H.W. performed the

cryo-EM experiments. W.Z. processed the CTF-corrected images. R.V. conducted the TEM image simulation. Z.Z., H.W., and N.R. conducted other characterizations. Yanbin Li, Yuzhang Li, W.Z., W.C., and Y.C. interpreted the results and co-wrote the paper. All authors discussed the results and commented on the manuscript.

## DECLARATION OF INTERESTS

The authors declare no competing interests.

Received: May 13, 2019

Revised: August 8, 2019

Accepted: August 21, 2019

Published: August 28, 2019

## REFERENCES

- Snaith, H.J. (2013). Perovskites: The emergence of a new era for low-cost, high-efficiency solar cells. *J. Phys. Chem. Lett.* **4**, 3623–3630.
- Green, M.A., and Ho-Baillie, A. (2017). Perovskite solar cells: The birth of a new era in photovoltaics. *ACS Energy Lett.* **2**, 822–830.
- Grätzel, M. (2017). The rise of highly efficient and stable perovskite solar cells. *Acc. Chem. Res.* **50**, 487–491.
- Correa-Baena, J.-P., Saliba, M., Buonassisi, T., Grätzel, M., Abate, A., Tress, W., and Hagfeldt, A. (2017). Promises and challenges of perovskite solar cells. *Science* **358**, 739–744.
- Kojima, A., Teshima, K., Shirai, Y., and Miyasaka, T. (2009). Organometal halide perovskites as visible-light sensitizers for photovoltaic cells. *J. Am. Chem. Soc.* **131**, 6050–6051.
- Berhe, T.A., Su, W.-N., Chen, C.-H., Pan, C.-J., Cheng, J.-H., Chen, H.-M., Tsai, M.-C., Chen, L.-Y., Dubale, A.A., and Hwang, B.-J. (2016). Organometal halide perovskite solar cells: degradation and stability. *Energy Environ. Sci.* **9**, 323–356.
- Wang, D., Wright, M., Elumalai, N.K., and Uddin, A. (2016). Stability of perovskite solar cells. *Sol. Energy Mater. Sol. Cells* **147**, 255–275.
- Grancini, G., and Nazeeruddin, M.K. (2019). Dimensional tailoring of hybrid perovskites for photovoltaics. *Nat. Rev. Mater.* **4**, 4–22.
- Diviti, G., Cacovich, S., Matteocci, F., Cinà, L., Di Carlo, A., and Ducati, C. (2016). In situ observation of heat-induced degradation of perovskite solar cells. *Nat. Energy* **1**, 15012.
- Li, Y., Xu, X., Wang, C., Ecker, B., Yang, J., Huang, J., and Gao, Y. (2017). Light-induced degradation of CH<sub>3</sub>NH<sub>3</sub>PbI<sub>3</sub> hybrid perovskite thin film. *J. Phys. Chem. C* **121**, 3904–3910.
- Leijtens, T., Eperon, G.E., Pathak, S., Abate, A., Lee, M.M., and Snaith, H.J. (2013). Overcoming ultraviolet light instability of sensitized TiO<sub>2</sub> with meso-superstructured organometal trihalide perovskite solar cells. *Nat. Commun.* **4**, 2885.
- Murugadoss, G., Tanaka, S., Mizuta, G., Kanaya, S., Nishino, H., Umeyama, T., Imahori, H., and Ito, S. (2015). Light stability tests of methylammonium and formamidinium Pb-halide perovskites for solar cell applications. *Jpn. J. Appl. Physiol.* **54**, 08KF08.
- De Bastiani, M., Dell’Erba, G., Gandini, M., D’Innocenzo, V., Neutzner, S., Kandada, A.R.S., Grancini, G., Binda, M., Prato, M., Ball, J.M., et al. (2016). Ion migration and the role of preconditioning cycles in the stabilization of the *J* - *V* characteristics of inverted hybrid perovskite solar cells. *Adv. Energy Mater.* **6**, 1501453.
- Aristidou, N., Eames, C., Sanchez-Molina, I., Bu, X., Kosco, J., Islam, M.S., and Haque, S.A. (2017). Fast oxygen diffusion and iodide defects mediate oxygen-induced degradation of perovskite solar cells. *Nat. Commun.* **8**, 15218.
- Hoke, E.T., Slotcavage, D.J., Dohner, E.R., Bowring, A.R., Karunadasa, H.I., and McGehee, M.D. (2015). Reversible photo-induced trap formation in mixed-halide hybrid perovskites for photovoltaics. *Chem. Sci. (Camb.)* **6**, 613–617.
- Leguy, A.M.A., Frost, J.M., McMahon, A.P., Sakai, V.G., Kochelmann, W., Law, C., Li, X., Foglia, F., Walsh, A., O’Regan, B.C., et al. (2015). The dynamics of methylammonium ions in hybrid organic-inorganic perovskite solar cells. *Nat. Commun.* **6**, 7124.
- Whitfield, P.S., Herron, N., Guise, W.E., Page, K., Cheng, Y.Q., Milas, I., and Crawford, M.K. (2016). Structures, phase transitions and tricritical behavior of the hybrid perovskite methyl ammonium lead iodide. *Sci. Rep.* **6**, 35685.
- Rothmann, M.U., Li, W., Zhu, Y., Bach, U., Spiccia, L., Etheridge, J., and Cheng, Y.-B. (2017). Direct observation of intrinsic twin domains in tetragonal CH<sub>3</sub>NH<sub>3</sub>PbI<sub>3</sub>. *Nat. Commun.* **8**, 14547.
- Chen, S., Zhang, X., Zhao, J., Zhang, Y., Kong, G., Li, Q., Li, N., Yu, Y., Xu, N., Zhang, J., et al. (2018). Atomic scale insights into structure instability and decomposition pathway of methylammonium lead iodide perovskite. *Nat. Commun.* **9**, 4807.
- Zhang, D., Zhu, Y., Liu, L., Ying, X., Hsiung, C.-E., Sougrat, R., Li, K., and Han, Y. (2018). Atomic-resolution transmission electron microscopy of electron beam-sensitive crystalline materials. *Science* **359**, 675–679.
- Li, Y., Li, Y., Pei, A., Yan, K., Sun, Y., Wu, C.-L., Joubert, L.-M., Chin, R., Koh, A.L., Yu, Y., et al. (2017). Atomic structure of sensitive battery materials and interfaces revealed by cryo-electron microscopy. *Science* **358**, 506–510.
- Wang, X., Zhang, M., Alvarado, J., Wang, S., Sina, M., Lu, B., Bouwer, J., Xu, W., Xiao, J., Zhang, J.-G., et al. (2017). New insights on the structure of electrochemically deposited lithium metal and its solid electrolyte interphases via Cryogenic TEM. *Nano Lett.* **17**, 7606–7612.
- Zachman, M.J., Tu, Z., Choudhury, S., Archer, L.A., and Kourkoutis, L.F. (2018). Cryo-STEM mapping of solid-liquid interfaces and dendrites in lithium-metal batteries. *Nature* **560**, 345–349.
- Li, Y., Huang, W., Li, Y., Pei, A., Boyle, D.T., and Cui, Y. (2018). Correlating structure and function of battery interphases at atomic resolution using cryoelectron microscopy. *Joule* **2**, 2167–2177.
- Li, Y., Li, Y., and Cui, Y. (2018). Catalyst: How Cryo-EM shapes the development of next-generation batteries. *Chem* **4**, 2250–2252.
- Li, Y., Wang, K., Zhou, W., Li, Y., Vila, R., Huang, W., Wang, H., Chen, G., Wu, G.H., Tsao, Y., et al. (2019). Cryo-EM structures of atomic surfaces and host-guest chemistry in metal-organic frameworks. *Matter* **1**, 1–11.
- McMeekin, D.P., Sadoughi, G., Rehman, W., Eperon, G.E., Saliba, M., Hörantner, M.T., Haghighirad, A., Sakai, N., Korte, L., Rech, B., et al. (2016). A mixed-cation lead mixed-halide perovskite absorber for tandem solar cells. *Science* **351**, 151–155.
- Olyaeefar, B., Ahmadi-Kandjani, S., and Asgari, A. (2018). Classical modelling of grain size and boundary effects in polycrystalline perovskite solar cells. *Sol. Energy Mater. Sol. Cells* **180**, 76–82.
- Shi, D., Adinolfi, V., Comin, R., Yuan, M., Alarousu, E., Buin, A., Chen, Y., Hoogland, S., Rothenberger, A., Katsiev, K., et al. (2015). Solar cells. Low trap-state density and long carrier diffusion in organolead trihalide perovskite single crystals. *Science* **347**, 519–522.

30. Park, N.G. (2016). Methodologies for high efficiency perovskite solar cells. *Nano Converg.* 3, 15.
31. Im, J.H., Luo, J., Franckevičius, M., Pellet, N., Gao, P., Moehl, T., Zakeeruddin, S.M., Nazeeruddin, M.K., Grätzel, M., and Park, N.G. (2015). Nanowire perovskite solar cell. *Nano Lett.* 15, 2120–2126.
32. Fu, Y., Meng, F., Rowley, M.B., Thompson, B.J., Shearer, M.J., Ma, D., Hamers, R.J., Wright, J.C., and Jin, S. (2015). Solution growth of single crystal methylammonium lead halide perovskite nanostructures for optoelectronic and photovoltaic applications. *J. Am. Chem. Soc.* 137, 5810–5818.
33. Liang, K., Mitzi, D.B., and Prikas, M.T. (1998). Synthesis and characterization of organic–inorganic perovskite thin films prepared using a versatile two-step dipping technique. *Chem. Mater.* 10, 403–411.
34. Chiu, W. (1986). Electron microscopy of frozen, hydrated biological specimens. *Annu. Rev. Biophys. Biophys. Chem.* 15, 237–257.
35. Li, X., Zheng, S.Q., Egami, K., Agard, D.A., and Cheng, Y. (2013). Influence of electron dose rate on electron counting images recorded with the K2 camera. *J. Struct. Biol.* 184, 251–260.
36. Li, X., Mooney, P., Zheng, S., Booth, C.R., Braunfeld, M.B., Gubbens, S., Agard, D.A., and Cheng, Y. (2013). Electron counting and beam-induced motion correction enable near-atomic-resolution single-particle cryo-EM. *Nat. Methods* 10, 584–590.
37. Hobbs, L.W. (1978). Radiation damage in electron microscopy of inorganic solids. *Ultramicroscopy* 3, 381–386.
38. Poglitsch, A., and Weber, D. (1987). Dynamic disorder in methylammoniumtrihalogenoplumbates (II) observed by millimeter-wave spectroscopy. *J. Chem. Phys.* 87, 6373–6378.
39. Baker, L.A., and Rubinstein, J.L. (2010). Radiation damage in electron cryomicroscopy. *Methods Enzymol.* 481, 371–388.
40. Bai, S., Da, P., Li, C., Wang, Z., Yuan, Z., Fu, F., Kawecki, M., Liu, X., Sakai, N., Wang, J.T.W., et al. (2019). Planar perovskite solar cells with long-term stability using ionic liquid additives. *Nature* 571, 245–250.
41. Bush, K.A., Bailie, C.D., Chen, Y., Bowring, A.R., Wang, W., Ma, W., Leijtens, T., Moghadam, F., and McGehee, M.D. (2016). Thermal and environmental stability of semi-transparent perovskite solar cells for tandems enabled by a solution-processed nanoparticle buffer layer and sputtered ITO electrode. *Adv. Mater.* 28, 3937–3943.
42. Shi, L., Young, T.L., Kim, J., Sheng, Y., Wang, L., Chen, Y., Feng, Z., Keevers, M.J., Hao, X., Verlinden, P.J., et al. (2017). Accelerated lifetime testing of organic–inorganic perovskite solar cells encapsulated by polyisobutylene. *ACS Appl. Mater. Interfaces* 9, 25073–25081.
43. Zheng, S.Q., Palovcak, E., Armache, J.-P., Verba, K.A., Cheng, Y., and Agard, D.A. (2017). MotionCor2: anisotropic correction of beam-induced motion for improved cryo-electron microscopy. *Nat. Methods* 14, 331–332.
44. Rohou, A., and Grigorieff, N. (2015). CTFIND4: Fast and accurate defocus estimation from electron micrographs. *J. Struct. Biol.* 192, 216–221.
45. Zhang, K. (2016). Gctf: Real-time CTF determination and correction. *J. Struct. Biol.* 193, 1–12.
46. Crowther, R.A., Henderson, R., and Smith, J.M. (1996). MRC image processing programs. *J. Struct. Biol.* 116, 9–16.
47. Biyani, N., Righetto, R.D., McLeod, R., Caujolle-Bert, D., Castano-Diez, D., Goldie, K.N., and Stahlberg, H. (2017). Focus: The interface between data collection and data processing in cryo-EM. *J. Struct. Biol.* 198, 124–133.
48. Kilaas, R. (1998). Optimal and near-optimal filters in high-resolution electron microscopy. *J. Microsc.* 190, 45–51.
49. Tang, G., Peng, L., Baldwin, P.R., Mann, D.S., Jiang, W., Rees, I., and Ludtke, S.J. (2007). EMAN2: an extensible image processing suite for electron microscopy. *J. Struct. Biol.* 157, 38–46.

**JOUL, Volume 3**

**Supplemental Information**

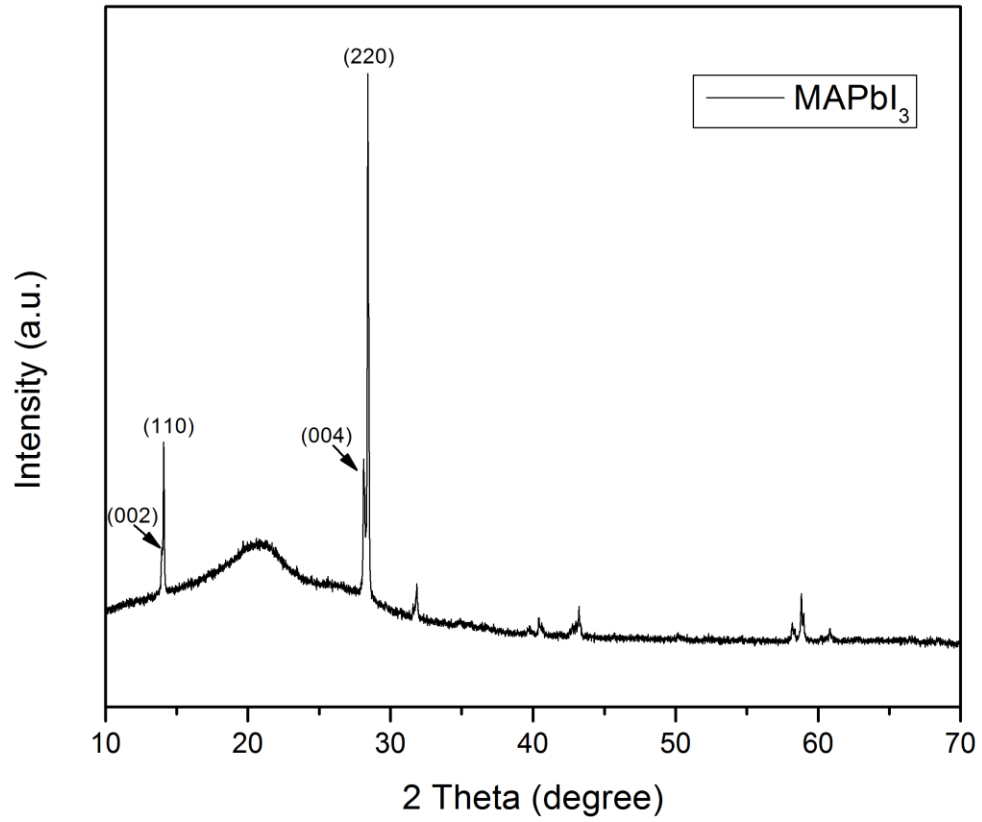
**Unravelling Degradation Mechanisms and**

**Atomic Structure of Organic-Inorganic**

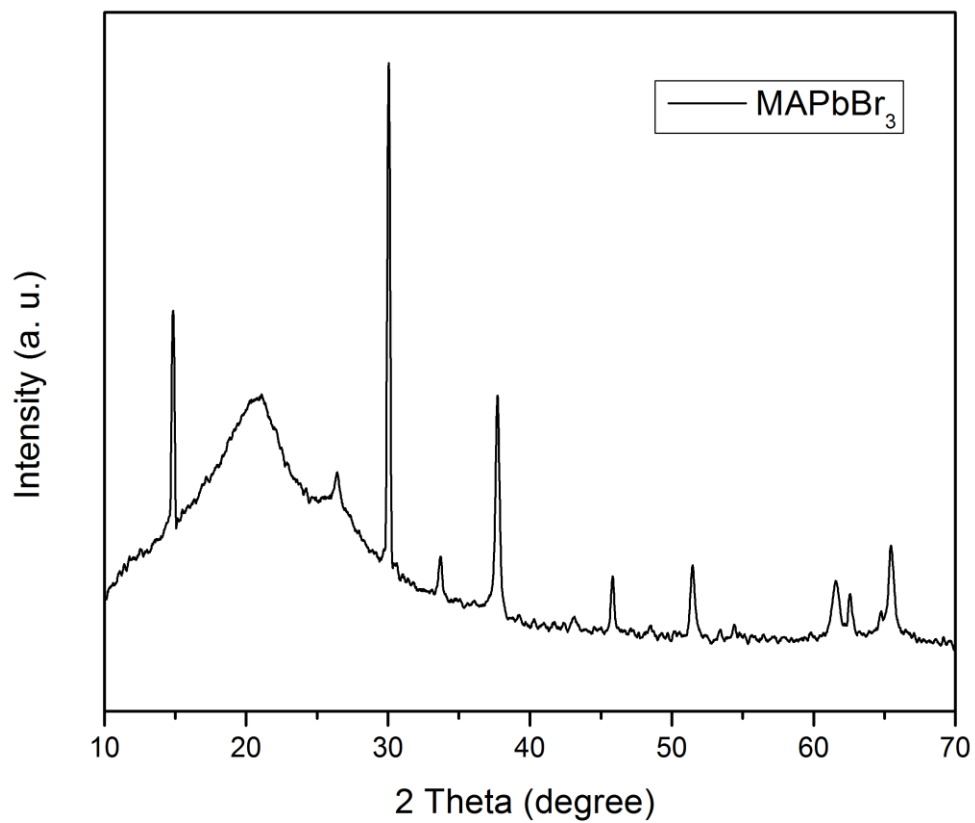
**Halide Perovskites by Cryo-EM**

**Yanbin Li, Weijiang Zhou, Yuzhang Li, Wenxiao Huang, Zewen Zhang, Guangxu Chen, Hansen Wang, Gong-Her Wu, Nicholas Rolston, Rafael Vila, Wah Chiu, and Yi Cui**

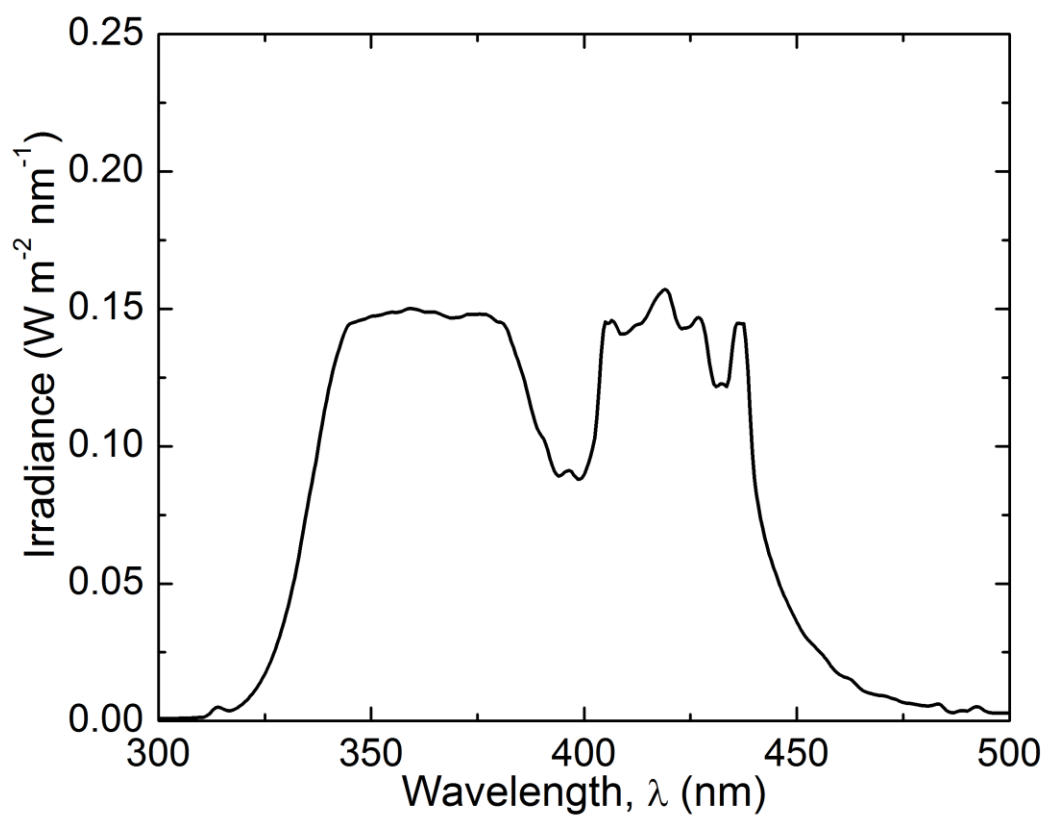
## Supplementary Figures



Supplementary Figure 1. X-ray diffraction (XRD) of pristine MAPbI<sub>3</sub> nanowires (NWs).

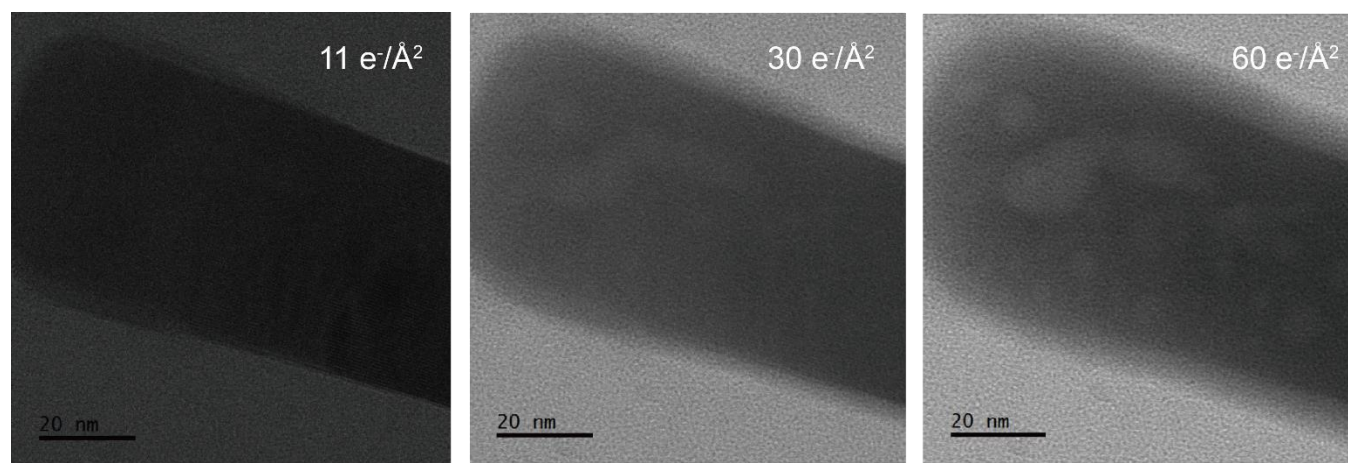


**Supplementary Figure 2. XRD of pristine MAPbBr<sub>3</sub> NWs.**



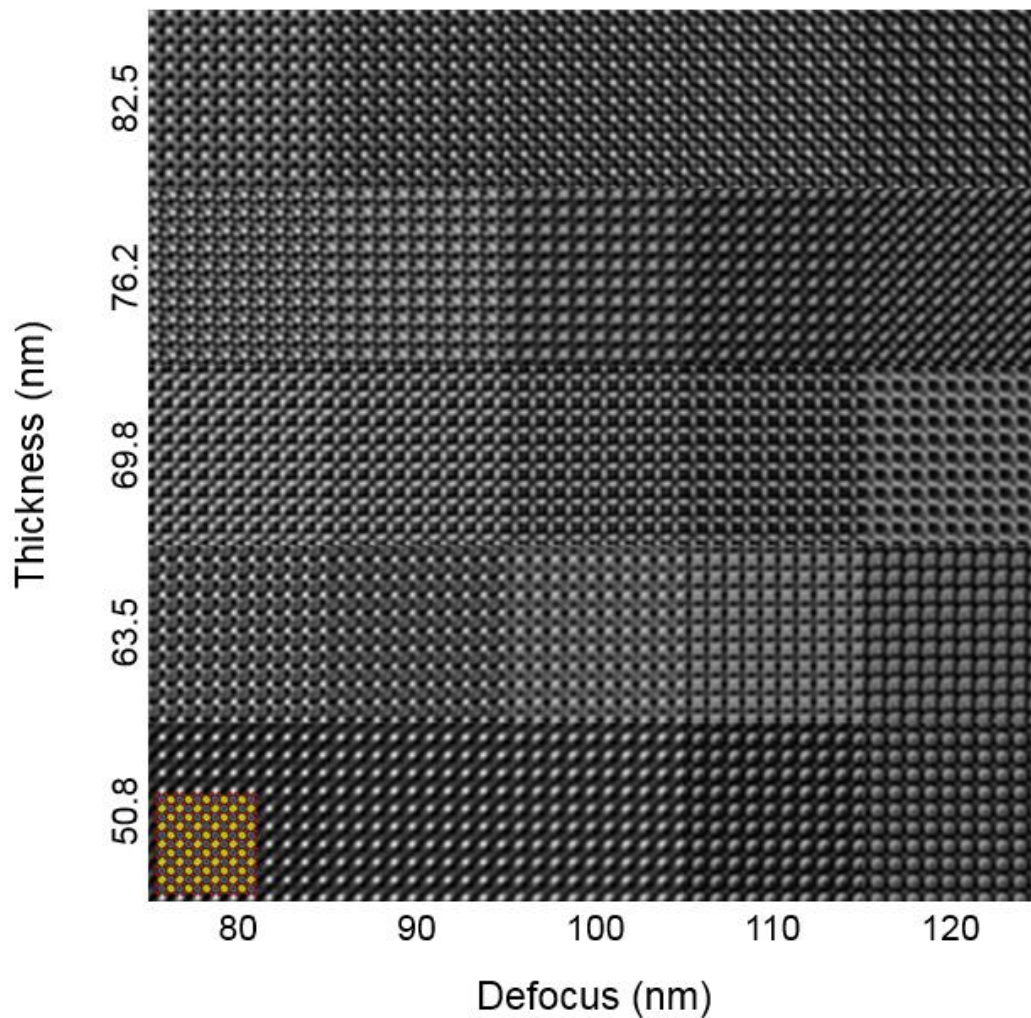
**Supplementary Figure 3. Irradiance spectrum of ultraviolet (UV) lamp used for UV degradation test.**

The spectral irradiance of the UV lamp was measured in a dark box using a SpectraWiz spectrometer with an integration time of 285 ms and an average of 5 spectra. The irradiance was integrated to obtain the intensity of 16.35 W m<sup>-2</sup> for the UV lamp, which is a broadband UVA source based on the spectral irradiance plot.



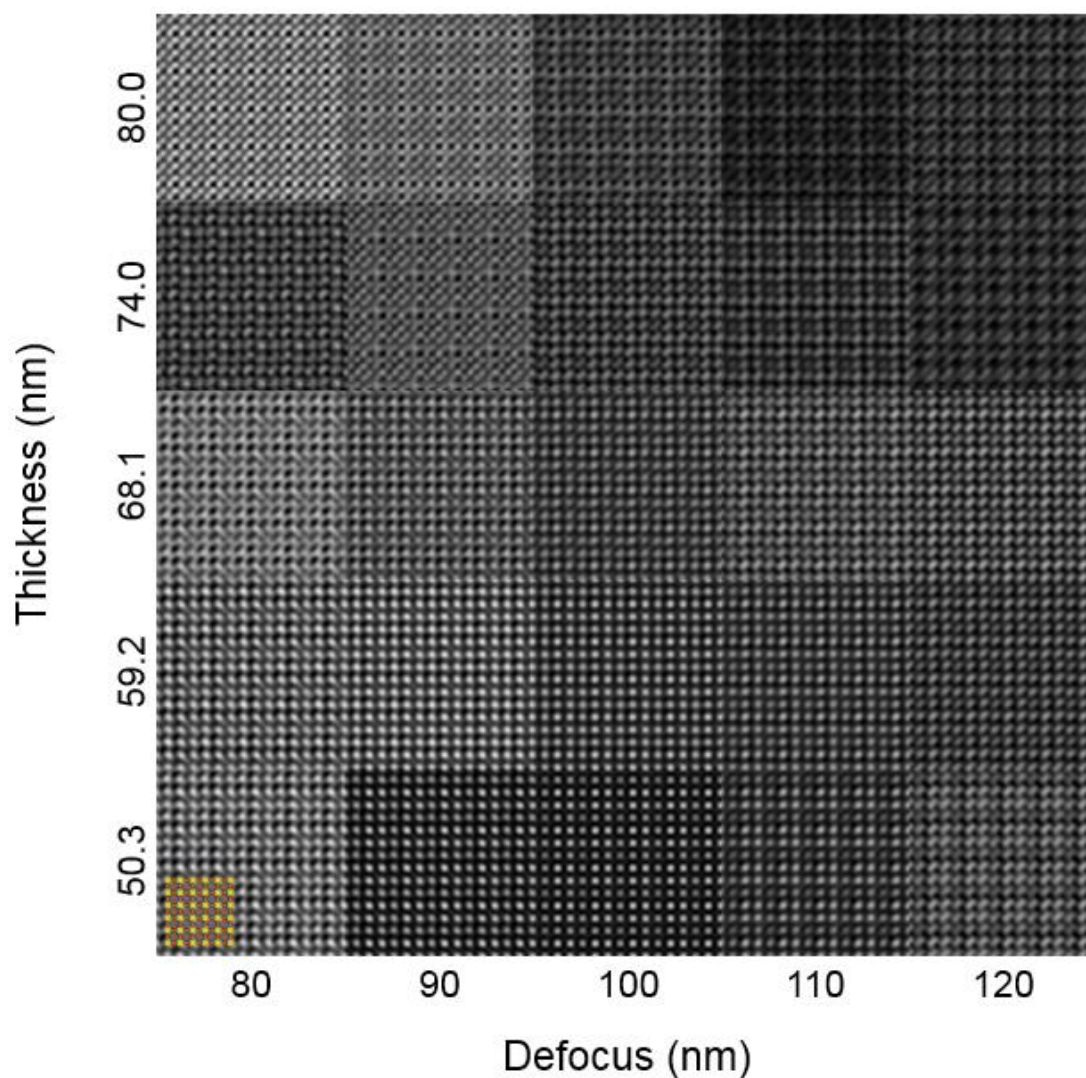
→  
continuous e<sup>-</sup> beam irradiation MAPbI<sub>3</sub> NWs

**Supplementary Figure 4. Continuous e beam irradiation on MAPbI<sub>3</sub> NWs forms bubbles.**



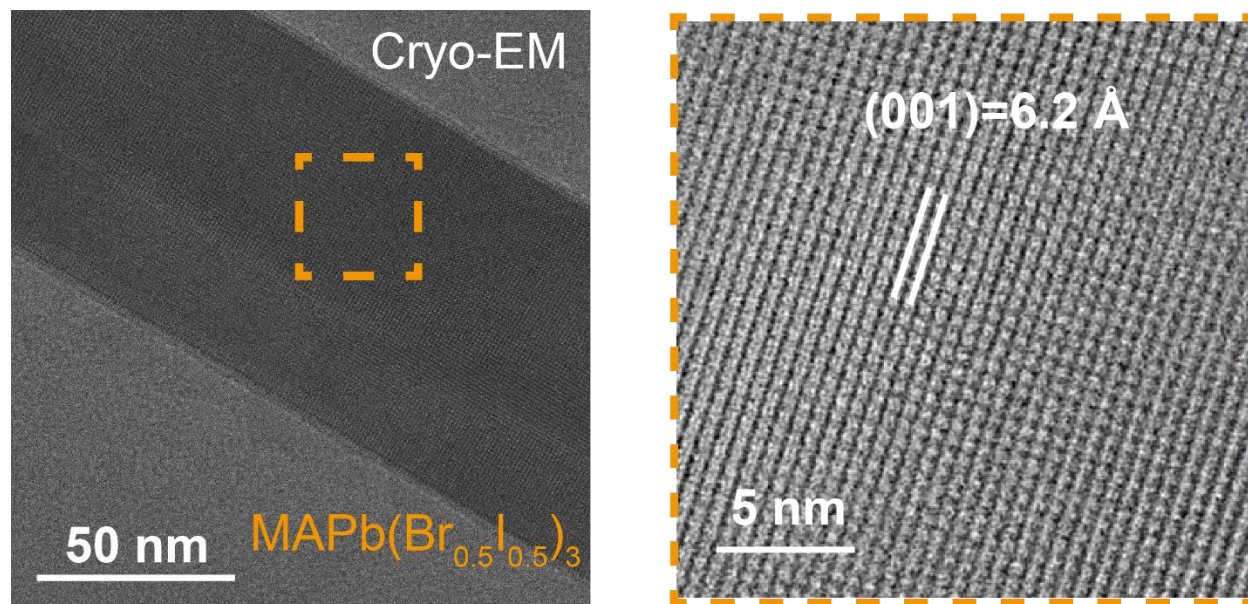
**Supplementary Figure 5. Image simulation of MAPbI<sub>3</sub> atomic positions along [001] zone axis.**

Simulated HRTEM images under image condition ( $C_s=1.2\text{mm}$ ), with varying focus values and crystal thicknesses. Simulated HRTEM images overlaid with atomic models. The yellow circles indicate the position of MA molecule columns. Overlaying images shows that, in most of cases, the bright spots represent the positions of MA molecule columns, indicating that the bright spots indeed correspond to MA molecule columns and that the HRTEM patterns are quite robust to defocus and thickness.



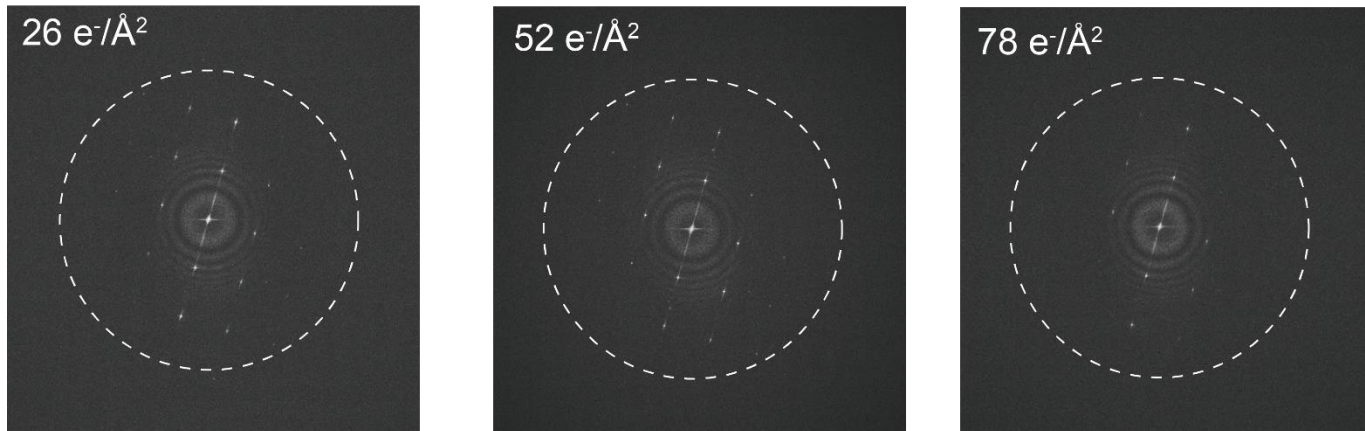
**Supplementary Figure 6. Image simulation of MAPbBr<sub>3</sub> atomic positions along [001] zone axis.**

Simulated HRTEM images under image condition ( $C_s=1.2\text{mm}$ ), with varying focus values and crystal thicknesses. Simulated HRTEM images overlaid with atomic models. The yellow circles indicate the position of MA molecule columns. Overlaying images shows that, in most of cases, the bright spots represent the positions of MA molecule columns, indicating that the bright spots indeed correspond to atomic columns and that the HRTEM patterns are quite robust to defocus and thickness



**Supplementary Figure 7. TEM images of  $\text{MAPb}(\text{Br}_{0.5}\text{I}_{0.5})_3$ .**

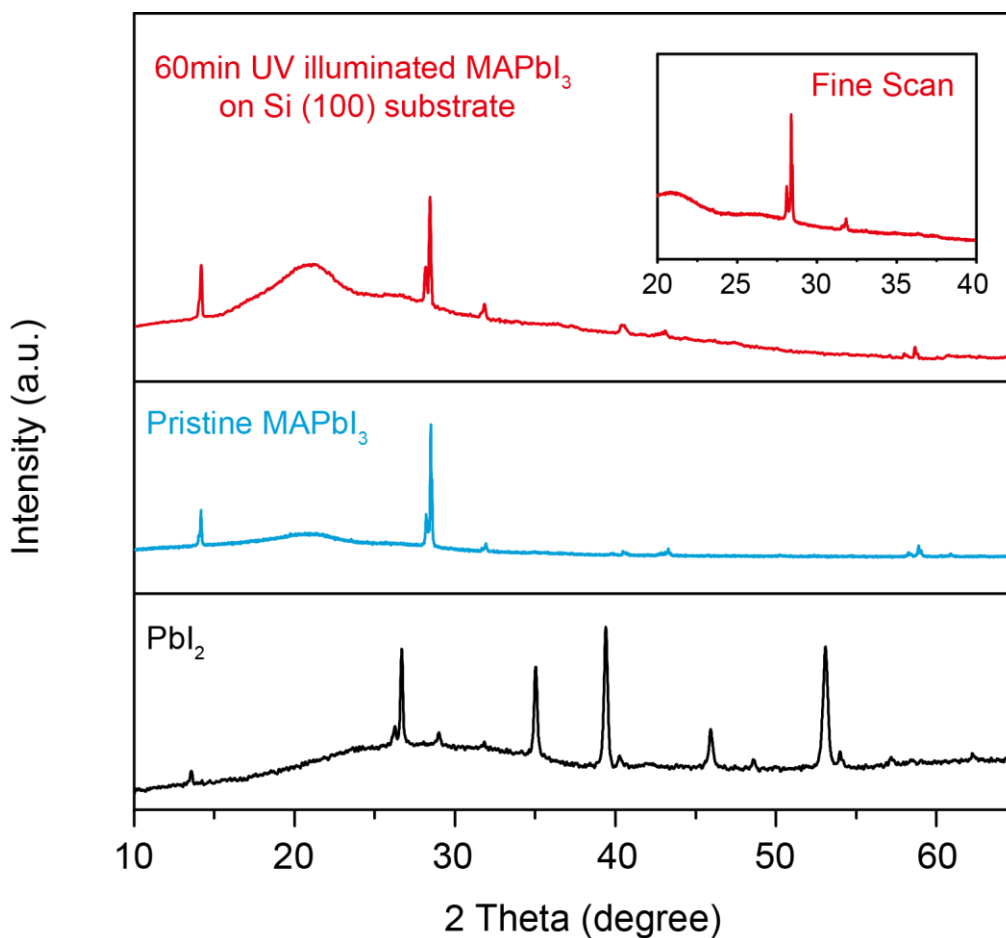
Electron dose is  $\sim 46 \text{ e}^-/\text{\AA}^2$



**Supplementary Figure 8. Radiation damage measurement on MAPbBr<sub>3</sub>**

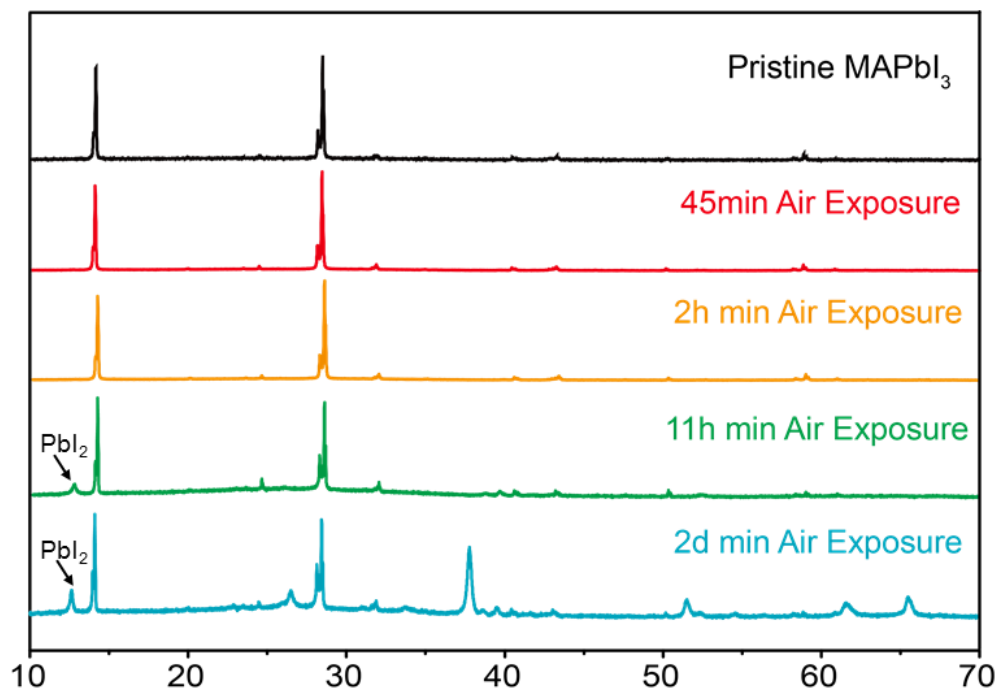
FFT of MAPbBr<sub>3</sub> HRTEM images with cumulative electron exposure 25.6 e<sup>-</sup>/Å<sup>2</sup>, 51.2 e<sup>-</sup>/Å<sup>2</sup> and 76.8 e<sup>-</sup>/Å<sup>2</sup>.

White circle represent an information of 2 Å.



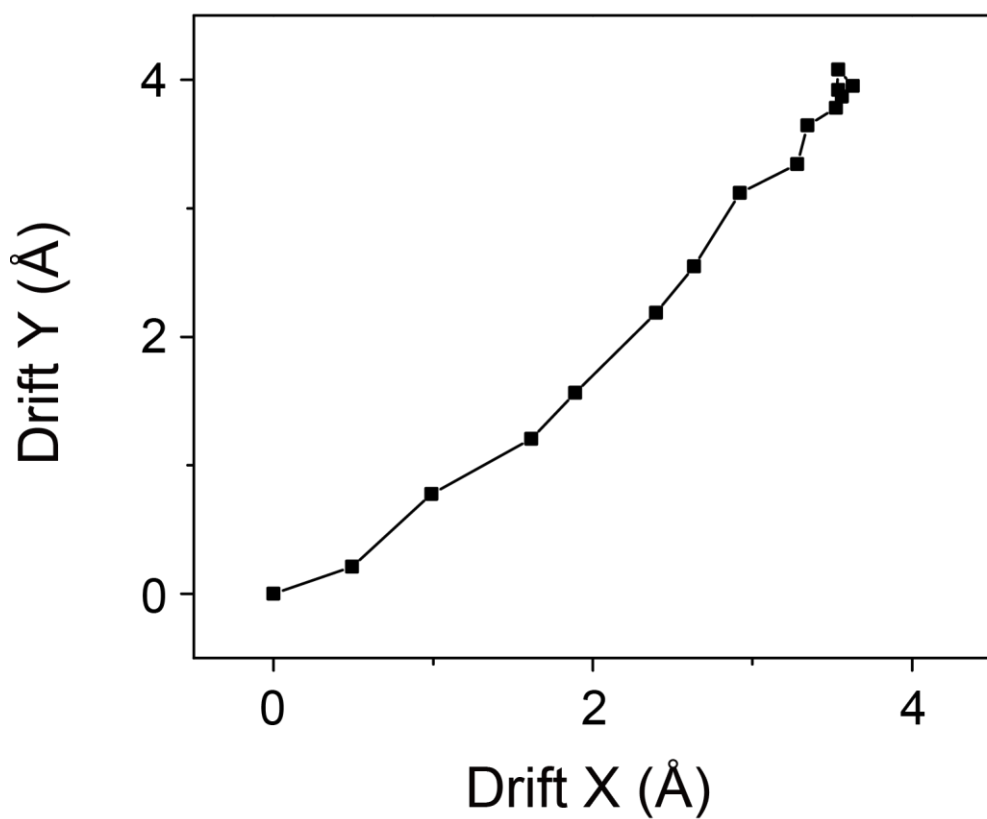
**Supplementary Figure 9. XRD of MAPbI<sub>3</sub> measured on silicon (100) substrate.** XRD spectra of 60min UV illuminated MAPbI<sub>3</sub> NWs on silicon substrate, pristine MAPbI<sub>3</sub> NWs and PbI<sub>2</sub>. (inset: Fine scan around PbI<sub>2</sub> peak positions).

Fine scan shows that no PbI<sub>2</sub> peak can be detected after 60 min UV illumination. XRD scanning for MAPbI<sub>3</sub> NWs on silicon (100) substrate was limited to 65 ° to avoid the strong diffraction from Si (400) peak.



**Supplementary Figure 10. MAPbI<sub>3</sub> degradation with 40% moisture exposure.**

XRD spectra of MAPbI<sub>3</sub> after 45 minutes, 2 hours, 11 hours, and 2 days of moisture exposure. Formation of PbI<sub>2</sub> is observable in XRD after 11 hours.



**Supplementary Figure 11. The image drift profile of MAPbI<sub>3</sub> HRTEM image in Figure 1 E and F.**

The trace shows that the initial small movement settles into a random motion. For comparison, the accumulated motion for biological sample (e.g. frozen hydrated *T. acidophilum* 20S proteasome embedded in vitreous ice) was around 2 Å. Thus, it's necessary to perform motion correction for MAPbI<sub>3</sub> NWs HRTEM imaging.